Progress In Electromagnetics Research B, Vol. 118, 104–118, 2026

PIER B

(Received 3 June 2026, Accepted 7 July 2026, Scheduled 14 August 2026)

Robust Resource Allocation for ORIS-Assisted VLC Networks under Random User Orientations

Zike Su, Wei Yang*, Xinru Wang, and Guangpeng Cheng

Institute of Intelligent Communication and Computing, School of Information and Communication Engineering
Beijing Information Science and Technology University, Beijing 102206, China

ABSTRACT: Random user orientation in indoor visible light communication (VLC) severely degrades the line-of-sight (LoS) channel and limits the gains of non-orthogonal multiple access (NOMA). This paper proposes a robust resource-allocation framework for an optical reconfigurable intelligent surface (ORIS)-assisted multi-cell VLC downlink under random Euler-angle user rotations. We fit truncated probability density functions (PDFs) for the LoS link and four ORIS links received by side-facing photodetectors (PDs) using Monte Carlo samples, maximum-likelihood estimation, and Akaike information criterion (AIC)-based model selection. Using this statistical channel-state information (CSI), we formulate a joint optical-power, user-association, and ORIS-activation problem that maximizes a weighted statistical-CSI rate surrogate under optical-power, eye-safety, quality-of-service, and physical-association constraints. A block-coordinate-descent (BCD) algorithm updates the three variable blocks using fractional programming, successive convex approximation, and semidefinite relaxation, respectively. Simulation results show gains of up to 14% and 56% over the proportional-allocation optimization (PAO) and time-division multiple-access (TDMA) baselines, respectively, at a signal-to-noise ratio (SNR) of 35 dB for the tested sitting-user orientation range $\sigma_\theta \leq 10^\circ$.

1. INTRODUCTION

With the rapid proliferation of sixth-generation (6G) mobile communications and Internet of Things (IoT) devices, traditional radio frequency (RF) spectrum resources are being depleted at an accelerated pace. Consequently, visible light communication (VLC) has emerged as a practical supplementary technology for broadband networks [1, 2]. VLC offers wide unlicensed spectrum bandwidth, strong immunity to electromagnetic interference, and dual capabilities of indoor illumination and data transmission [3]. Nevertheless, realizing high throughput and dense connectivity in complex indoor environments requires systematic improvements to existing VLC architectures.

To enhance spectral efficiency and support concurrent multi-user access, non-orthogonal multiple access (NOMA) has been integrated into VLC networks via power-domain multiplexing [4, 5]. However, VLC propagation is highly directional and inherently relies on line-of-sight (LoS), making it susceptible to obstructions and beam misalignment. To restructure the indoor optical propagation environment, optical reconfigurable intelligent surfaces (ORISs) have been recently introduced as low-complexity passive reflective arrays that establish auxiliary non-line-of-sight (NLoS) links for edge users [6–8].

Despite these advances, the angular sensitivity of the photodetector remains the dominant bottleneck of indoor VLC: hand-held terminals continually rotate, and even modest yaw/pitch deviations induce dB-scale fades along the LoS path. Empirical studies [9, 10] report that the per-link incidence-cosine over typical sitting/walking sessions is well captured by truncated Laplace and Gaussian densities derived from Euler-angle perturbations. Yet, despite extensive measurements of receiver-orientation statistics, most existing ORIS-assisted resource-allocation frameworks [5, 11–13] assume a fixed vertical receiver normal, leaving the joint impact of orientation randomness on power allocation, user association, and ORIS activation largely unexplored.

Existing NOMA-VLC allocation studies usually assume a fixed receiver. ORIS-assisted studies also tend to use deterministic or instantaneous channel information. In contrast, measurement studies describe random receiver orientation but do not optimize NOMA and ORIS resources. This work connects these directions by using orientation statistics in a joint optical-power, user-association, and ORIS-activation design. The three variable blocks are updated by fractional programming [14, 15], successive convex approximation (SCA) [11], and semidefinite relaxation (SDR) [13, 16]. Table 1 gives a concise comparison.

Motivated by these practical challenges, this paper considers an ORIS-assisted multi-cell VLC downlink in which J users undergo random Euler-angle rotations and develops a tractable robust resource-allocation framework that explicitly leverages statistical channel-state information (CSI). In contrast to existing works, the main contributions of this paper are summarized as follows:

1) *Analytical channel statistical modeling*: We derive closed-form probability density functions (PDFs) for the channel gains of direct LoS links and ORIS-assisted reflection links under random user orientations (utilizing Euler angle rotations). This statistical model quantifies orientation-induced signal fading without relying on instantaneous channel state information (CSI).

* Corresponding author: Wei Yang (ywiaia009@bistu.edu.cn).

TABLE 1. Comparison with representative VLC research directions.

Study group	Receiver orientation	ORIS model	Main scope
NOMA-VLC allocation [4, 5]	Fixed	Not considered	Power and user allocation
ORIS/RIS-assisted VLC [11–13, 16]	Usually fixed	Deterministic reflected links	Power, association, and reflection control
Orientation modeling in VLC [9, 10]	Measurement-based random orientation	Not considered	Channel statistics
This work	Random Euler-angle orientation	Statistical LoS and ORIS links	Joint optical power, association, and ORIS activation

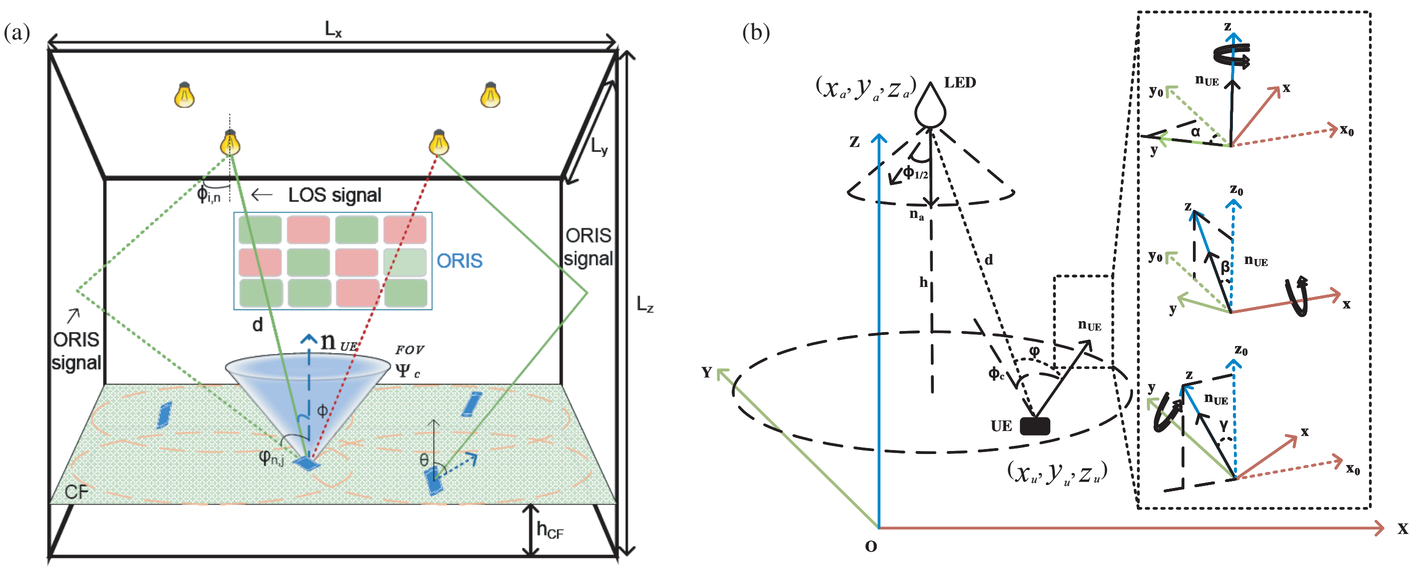

Scenario diagram of a multi-building indoor visible light communication system model

3D Schematic of the User Receiver End

FIGURE 1. System model of the considered ORIS-assisted multi-user indoor VLC downlink: (a) overall scenario and (b) 3D geometry of a randomly-oriented receiver with one top-facing and four side-facing photodetectors (PDs).

2) *Joint optimization framework*: We formulate an ORIS-assisted resource-allocation mixed-integer nonlinear programming (MINLP) that maximizes a statistical-CSI rate surrogate. The framework jointly optimizes optical power, user association, and discrete ORIS activation under power, eye-safety, quality of service (QoS), and physical-association constraints.

3) *Tractable iterative solution algorithm*: To solve the coupled non-convex problem, we develop an alternating algorithm based on block coordinate descent (BCD). The formulation is decoupled into three subproblems, which are sequentially resolved using fractional programming (FP) for power allocation, successive convex approximation (SCA) for user association, and semidefinite relaxation (SDR) with Gaussian randomization for ORIS activation.

4) *ORIS-aware successive interference cancellation (SIC) adaptation*: Each ORIS update changes the composite statistical channel. The SIC order is therefore recomputed before the next power-allocation update, allowing the reflection and NOMA decisions to adapt jointly.

5) *Performance evaluation*: Numerical simulations compare the fitted channel statistics and evaluate the optimization framework for sitting or mildly moving users. The results show that ORIS-assisted links reduce orientation-induced attenuation over the tested range.

The remainder of this paper is organized as follows. Section 2 presents the system models for the multi-user VLC architecture, characterizing the spatial orientation states of the LoS and ORIS links. Section 3 formulates the joint resource allocation optimization problem alongside its mathematical constraints. Section 4 details the proposed BCD-based iterative algorithm. Section 5 provides the numerical results and performance evaluations. Finally, Section 6 concludes the paper.

2. SYSTEM MODEL

As shown in Fig. 1(a), we consider a $5 \times 5 \times 3\,\mathrm{m}^3$ room containing I ceiling light-emitting diodes (LEDs), N ORIS reflecting units distributed across the four walls, and J mobile users. Define the index sets $\mathscr{I} \triangleq \{1, \ldots, I\}$, $\mathscr{N} \triangleq \{1, \ldots, N\}$, and $\mathscr{J} \triangleq \{1, \ldots, J\}$. The position vectors of LED i, ORIS unit

n, and user j are $\mathbf{r}_i$, $\mathbf{r}_n$, and $\mathbf{r}_j$, respectively. The optimization variables are the optical-power matrix $\mathbf{P} = [p_{i,j}] \in \mathbb{R}_+^{I\times J}$, the association matrix $\mathbf{F} = [f_{i,j}] \in \{0,1\}^{I\times J}$, and the ORIS activation tensor $\mathbf{Q} = [q_{i,n,j}] \in \{0,1\}^{I\times N\times J}$.

As illustrated in Fig. 1(b), unlike most existing studies, which assume a vertically oriented receiver with its normal pointing toward the ceiling, this paper considers random holding orientations of the user equipment. The receiver state is described by its three-dimensional position and the normal vector of each photodetector (PD). To represent practical user behavior, we adopt a decoupled quasi-static position and dynamic-orientation model:

1) Quasi-static user position: Because indoor users typically move slowly and the millisecond-scale resource-allocation interval is much shorter than the time scale of macroscopic displacement, each user's position is treated as constant within a scheduling interval. Thus, every user has fixed three-dimensional coordinates during one optimization process [5].
2) Random orientation: The position is fixed during one scheduling interval, while the device normal varies with the Euler-angle vector $\boldsymbol{\xi} = [\alpha, \beta, \gamma]^T$. The Z-X-Y matrix $\mathbf{R}(\boldsymbol{\xi})$ maps each local PD normal to the room coordinate system. We focus on the sitting-user statistics reported in [9], for which orientation changes are concentrated around a nominal posture.

Using the Z-X-Y rotation convention,

$$\mathbf{R} = \mathbf{R}_z\,(\text{yaw}) \cdot \mathbf{R}_x\,(\text{roll}) \cdot \mathbf{R}_y\,(\text{pitch})\,, \tag{1}$$

The top-facing PD has local normal $\mathbf{n}_0 = [0, 0, 1]^T$. Its global normal is $\mathbf{n}_{\text{UE}} = \mathbf{R}\mathbf{n}_0$.

2.1. LoS Path Channel Statistics

For the LoS link emitted from the source LED, when the device is rotated, the normal vector becomes as detailed in Eq. (2):

$$\begin{aligned}
\overrightarrow{n_{\text{UE}}} &= \mathbf{R}_\alpha \mathbf{R}_\beta \mathbf{R}_\gamma \begin{bmatrix} 0 \\ 0 \\ 1 \end{bmatrix} \\
&= \begin{bmatrix} \cos\alpha & -\sin\alpha & 0 \\ \sin\alpha & \cos\alpha & 0 \\ 0 & 0 & 1 \end{bmatrix} \begin{bmatrix} 1 & 0 & 0 \\ 0 & \cos\beta & -\sin\beta \\ 0 & \sin\beta & \cos\beta \end{bmatrix} \\
&\quad \begin{bmatrix} \cos\gamma & 0 & \sin\gamma \\ 0 & 1 & 0 \\ -\sin\gamma & 0 & \cos\gamma \end{bmatrix} \begin{bmatrix} 0 \\ 0 \\ 1 \end{bmatrix} \\
&= \begin{bmatrix} \cos\gamma\sin\alpha\sin\beta + \cos\alpha\sin\gamma \\ \sin\alpha\sin\gamma - \cos\alpha\cos\gamma\sin\beta \\ \cos\beta\cos\gamma \end{bmatrix}.
\end{aligned} \tag{2}$$

Let θ and ζ denote the polar and azimuth angles of the top-facing PD, respectively. Its unit normal can equivalently be written as

$$\mathbf{n}_{\text{UE}}(\theta, \zeta) = \begin{bmatrix} \sin\theta\cos\zeta \\ \sin\theta\sin\zeta \\ \cos\theta \end{bmatrix}, \tag{3}$$

According to Eqs. (2)–(3), the two angles are determined by the Euler triplet (α, β, γ) as

$$\begin{aligned}
\theta &= \cos^{-1}(\cos\beta\cos\gamma), \\
\zeta &= \operatorname{atan2}\big(\sin\alpha\sin\gamma - \cos\alpha\cos\gamma\sin\beta, \\
&\qquad \cos\gamma\sin\alpha\sin\beta + \cos\alpha\sin\gamma\big),
\end{aligned} \tag{4}$$

Thus, θ depends on (β, γ), and ζ depends on all three Euler angles. We do not assume that these angles are analytically independent. Instead, their joint effect is retained when Euler-angle samples are transformed into channel samples. For the scalar LoS approximation below, the measured marginal distribution of θ is represented by a Laplace density truncated to $[\theta_{\min}, \theta_{\max}]$ [10]:

$$f_\theta(\theta) = \frac{\exp\left(-|\theta - \mu_\theta|/b_\theta\right)}{2b_\theta Z_\theta}, \quad \theta \in [\theta_{\min}, \theta_{\max}], \tag{5}$$

where $Z_\theta = F_{\text{Lap}}(\theta_{\max}; \mu_\theta, b_\theta) - F_{\text{Lap}}(\theta_{\min}; \mu_\theta, b_\theta)$, μ_θ is the measured sitting-posture mean, and b_θ is the Laplace scale. The untruncated variance is $\sigma_\theta^2 = 2b_\theta^2$. The LoS incidence cosine is

$$\cos\varphi = \frac{\overrightarrow{d}}{|\overrightarrow{d}|} \cdot \mathbf{n}_{\text{UE}} = \frac{\overrightarrow{d}}{|\overrightarrow{d}|} \cdot \mathbf{R}\mathbf{n}_0, \tag{6}$$

where $|\overrightarrow{d}|$ represents the Euclidean distance between access point (AP) and user equipment (UE). Denoting the access-point (LED) and user positions as (x_a, y_a, z_a) and (x_u, y_u, z_u) respectively, the cosine of the incident angle can be expressed as in Eq. (7):

$$\begin{aligned}
X \;\triangleq\; \cos\varphi &= \left(\frac{x_a - x_u}{|\overrightarrow{d}|}\right)\sin\theta\cos\zeta \\
&\quad + \left(\frac{y_a - y_u}{|\overrightarrow{d}|}\right)\sin\theta\sin\zeta + \left(\frac{z_a - z_u}{|\overrightarrow{d}|}\right)\cos\theta,
\end{aligned} \tag{7}$$

Eq. (7) characterizes the geometry of the LoS link. Here, parameters a and b are introduced to facilitate subsequent calculations, as defined in Eq. (8):

$$\begin{aligned}
a &\triangleq \left(\frac{x_a - x_u}{|\overrightarrow{d}|}\right)\cos\zeta + \left(\frac{y_a - y_u}{|\overrightarrow{d}|}\right)\sin\zeta, \\
b &\triangleq \left(\frac{z_a - z_u}{|\overrightarrow{d}|}\right),
\end{aligned} \tag{8}$$

The first-order Taylor expansion approximation of $\cos\varphi$ at $\theta = \mu_\theta$ is performed under the condition that the variance of θ is small, yielding Eq. (9):

$$\cos\varphi \approx a\sin\mu_\theta + b\cos\mu_\theta + (a\cos\mu_\theta - b\sin\mu_\theta)\cdot(\theta - \mu_\theta), \tag{9}$$

By assigning the coefficients in Eq. (9) to variables as seen in Eq. (10):

$$\begin{cases} \mu_{\cos\varphi} = a\sin\mu_\theta + b\cos\mu_\theta \\ \ell_\theta = a\cos\mu_\theta - b\sin\mu_\theta \end{cases}, \tag{10}$$

$$\cos\varphi \approx \mu_{\cos\varphi} + \ell_\theta \cdot (\theta - \mu_\theta), \tag{11}$$

Equation (11) gives a scalar first-order approximation for the LoS incidence cosine. Conditional on a positive incidence cosine, its continuous density is approximated by a Laplace law on $x \in [0, 1]$:

$$f_{\cos\varphi}(x) = \frac{1}{Z_{\text{LoS}}} \cdot \frac{1}{2|\ell_\theta|b_\theta} \exp\left(-\frac{|x - \mu_{\cos\varphi}|}{|\ell_\theta|b_\theta}\right), \quad x \in [0, 1], \tag{12}$$

Here, $Z_{\text{LoS}} = F_{\text{Lap}}(1; \mu_{\cos\varphi}, |\ell_\theta|b_\theta) - F_{\text{Lap}}(0; \mu_{\cos\varphi}, |\ell_\theta|b_\theta)$. This conditional density is used for curve fitting only. Channel-moment calculations retain all Euler-angle samples and set the channel to zero whenever $\cos\varphi < \cos\psi_c$, so field-of-view (FoV) outages are not removed by renormalization.

2.2. ORIS-Reflected Path Channel Statistics

For the ORIS-assisted NLoS links, the ORIS arrays are distributed on the four side walls. To fully exploit the spatial diversity provided by the distributed ORISs, we assume that the UE is equipped with an angular diversity receiver (ADR) consisting of multiple photodetectors (PDs) [17]. In addition to the top-facing PD dedicated to the LoS path, four supplementary PDs are mounted on the UE and tilted at selected angles (e.g., 45 degrees) toward the four walls to capture the ORIS-reflected signals. The initial local normal vectors of these four side-facing PDs in the device coordinate system are defined as $\vec{n}_{\text{r,ORIS}_1} = [0, 1, 1]^T$, $\vec{n}_{\text{r,ORIS}_2} = [1, 0, 1]^T$, $\vec{n}_{\text{r,ORIS}_3} = [0, -1, 1]^T$, and $\vec{n}_{\text{r,ORIS}_4} = [-1, 0, 1]^T$, respectively. All side-facing PDs undergo the same rotation $\mathbf{R}(\boldsymbol{\xi})$. Their raw local normals have norm $\sqrt{2}$, so each is normalized before rotation. The resulting global unit normals are

$$\begin{aligned}
\vec{n}_r^{ORIS_1} &= \frac{1}{\sqrt{2}} \begin{bmatrix} -\sin\alpha\cos\beta + \cos\alpha\sin\gamma + \sin\alpha\sin\beta\cos\gamma \\ \cos\alpha\cos\beta + \sin\alpha\sin\gamma - \cos\alpha\sin\beta\cos\gamma \\ \sin\beta + \cos\beta\cos\gamma \end{bmatrix} \\
\vec{n}_r^{ORIS_2} &= \frac{1}{\sqrt{2}} \begin{bmatrix} \cos\alpha(\cos\gamma + \sin\gamma) + \sin\alpha\sin\beta(\cos\gamma - \sin\gamma) \\ \sin\alpha(\cos\gamma + \sin\gamma) - \cos\alpha\sin\beta(\cos\gamma - \sin\gamma) \\ \cos\beta(\cos\gamma - \sin\gamma) \end{bmatrix} \\
\vec{n}_r^{ORIS_3} &= \frac{1}{\sqrt{2}} \begin{bmatrix} \sin\alpha\cos\beta + \cos\alpha\sin\gamma + \sin\alpha\sin\beta\cos\gamma \\ -\cos\alpha\cos\beta + \sin\alpha\sin\gamma - \cos\alpha\sin\beta\cos\gamma \\ -\sin\beta + \cos\beta\cos\gamma \end{bmatrix} \\
\vec{n}_r^{ORIS_4} &= \frac{1}{\sqrt{2}} \begin{bmatrix} \cos\alpha(\sin\gamma - \cos\gamma) + \sin\alpha\sin\beta(\sin\gamma + \cos\gamma) \\ \sin\alpha(\sin\gamma - \cos\gamma) - \cos\alpha\sin\beta(\sin\gamma + \cos\gamma) \\ \cos\beta(\sin\gamma + \cos\gamma) \end{bmatrix}.
\end{aligned} \tag{13}$$

Similarly, we define the equivalent polar angles θ_{ORIS_1}, θ_{ORIS_2}, θ_{ORIS_3}, θ_{ORIS_4}, which represent the corresponding angles between the rotated unit normal vectors of the side-facing PDs and the positive Z-axis, i.e., $\theta_{ORIS_k} = \cos^{-1}([\vec{n}_r^{ORIS_k}]_z)$. Substituting the third component of each unit normal vector in Eq. (13), the polar angle of the specific PD associated with each ORIS link can be formulated as:

$$\begin{aligned}
\theta_{\text{ORIS}_1} &= \cos^{-1}\left(\tfrac{\sin\beta + \cos\beta\cos\gamma}{\sqrt{2}}\right) \\
\theta_{\text{ORIS}_2} &= \cos^{-1}\left(\tfrac{\cos\beta(\cos\gamma - \sin\gamma)}{\sqrt{2}}\right) \\
\theta_{\text{ORIS}_3} &= \cos^{-1}\left(\tfrac{-\sin\beta + \cos\beta\cos\gamma}{\sqrt{2}}\right) \\
\theta_{\text{ORIS}_4} &= \cos^{-1}\left(\tfrac{\cos\beta(\sin\gamma + \cos\gamma)}{\sqrt{2}}\right)
\end{aligned} \tag{14}$$

Compared with the formulation in [18], Eqs. (13) and (14) explicitly normalize the side-PD normal vectors by $\sqrt{2}$ to guarantee a valid polar-angle domain. We also re-derive the z-components of $\vec{n}_r^{ORIS_1}$ and $\vec{n}_r^{ORIS_2}$ to ensure consistency with the coordinate convention adopted here. These amendments ensure mathematical self-consistency for the subsequent statistical fitting without altering the overall analytical framework.

The polar angle alone is insufficient to determine the incidence angle of a side-facing PD. Let $\mathbf{n}_{0,k}$ be the normalized local normal of side PD $k \in \{1, 2, 3, 4\}$, and let $\widehat{\mathbf{d}}_{n,j} = (\mathbf{r}_n - \mathbf{r}_j)/\|\mathbf{r}_n - \mathbf{r}_j\|$ be the unit vector from user j to ORIS unit n. The incidence cosine is computed directly from the rotated three-dimensional normal:

$$X_{k,n,j}(\boldsymbol{\xi}) \triangleq \cos\varphi_{k,n,j} = \widehat{\mathbf{d}}_{n,j}^T \mathbf{R}(\alpha, \beta, \gamma)\mathbf{n}_{0,k}, \quad \boldsymbol{\xi} = [\alpha, \beta, \gamma]^T. \tag{15}$$

We generate channel samples from the joint Euler-angle model and fit simple marginal distributions for analytical evaluation. Following [9], the orientation perturbation is modeled as a three-dimensional Gaussian around a nominal sitting posture:

$$f_{\boldsymbol{\xi}}(\boldsymbol{\xi}) = \frac{\exp\left[-\frac{1}{2}(\boldsymbol{\xi} - \bar{\boldsymbol{\xi}})^T \boldsymbol{\Sigma}^{-1}(\boldsymbol{\xi} - \bar{\boldsymbol{\xi}})\right]}{(2\pi)^{3/2}\det(\boldsymbol{\Sigma})^{1/2}} \tag{16}$$

Here, $\bar{\boldsymbol{\xi}}$ is the nominal Euler posture, and $\boldsymbol{\Sigma}$ is the covariance matrix of the zero-mean perturbation $\delta\boldsymbol{\xi} = \boldsymbol{\xi} - \bar{\boldsymbol{\xi}}$. The nominal posture is calibrated so that the induced top-PD polar-angle mean agrees with the measured value μ_θ in Table 3; the Euler angles themselves are therefore not asserted to have zero absolute mean. For each side PD, 10^6 Euler samples are transformed through Eq. (15). AIC selects a model from truncated Gaussian, double-Gaussian, Weibull, Rayleigh, and Laplace candidates, and maximum likelihood estimation (MLE) estimates its parameters.

For small perturbations, the direct incidence-cosine mapping has the multivariate first-order approximation

$$X_{k,n,j}(\boldsymbol{\xi}) \approx X_{k,n,j}(\bar{\boldsymbol{\xi}}) + \nabla_{\boldsymbol{\xi}} X_{k,n,j}(\boldsymbol{\xi})|_{\bar{\boldsymbol{\xi}}}^T \,\delta\boldsymbol{\xi}. \tag{17}$$

The physical ORIS channel retains the FoV outage rather than conditioning it away:

$$H_{i,n,j}^{\text{ORIS}}(\boldsymbol{\xi}) = K_{i,n,j}^{\text{ORIS}} X_{k,n,j}(\boldsymbol{\xi}) \mathbb{I}\left\{X_{k,n,j}(\boldsymbol{\xi}) \geq \cos\psi_c\right\}, \tag{18}$$

Here, $\mathbb{I}\{\mathscr{A}\}$ denotes the indicator function: it equals 1 when event $\mathscr{A}$ holds and 0 otherwise; $K_{i,n,j}^{\text{ORIS}}$ collects the deterministic geometric and optical factors.

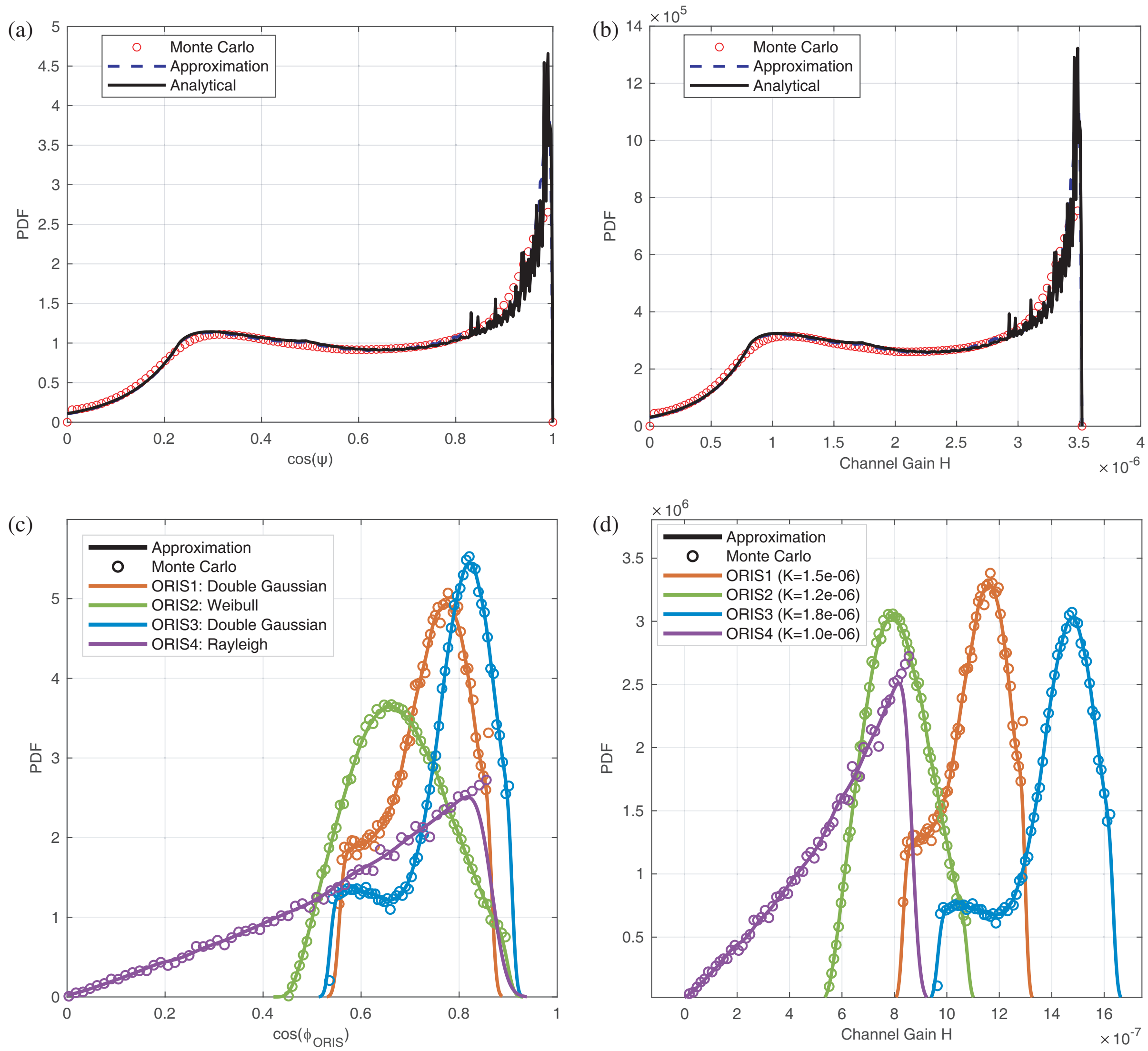

FIGURE 2. (a) and (b) show the distribution fitting of the cosine of the incident angle and the channel gain for the LoS path, respectively. (c) and (d) show the distribution fitting of the cosine of the incident angle and the channel gain for the four ORIS-reflected paths, respectively.

The Taylor remainder is second order in $\|\delta\boldsymbol{\xi}\|$. Because its numerical value depends on geometry and covariance, the fitted curves in Fig. 2 are used to assess the approximation over the tested sitting-user range, instead of claiming a geometry-independent scalar error bound.

The above accuracy should be interpreted within the sitting or mildly moving orientation regime. If the terminal undergoes abrupt rotations, non-stationary hand motion, or walking-induced posture changes with substantially larger angular variance, the fitted parameters in Table 4 should be re-estimated from the corresponding orientation traces and the first-order mapping may need to be replaced by a higher-order or purely sample-average channel model. This limitation is consistent with the measurement-driven nature of the adopted orientation statistics.

The continuous fitted densities below describe positive incidence-cosine samples on $x \in [0,1]$, with normalizer $Z_k = \int_0^1 \widetilde{f}_{X_k}(x)\,\mathrm{d}x$. They support compact analytical comparisons, but the second-order channel moments used by the optimizer are evaluated using the original Euler samples with the FoV indicator in Eq. (18). Thus, samples outside the FoV contribute zero channel gain rather than being discarded.

1) *ORIS 1*: MLE-AIC selects a truncated double-Gaussian model:

$$f_{\cos\varphi_1}(x) = \frac{1}{Z_1}\left[\frac{w_1}{\sqrt{2\pi}\sigma_1} e^{-\frac{(x-\mu_1)^2}{2\sigma_1^2}} + \frac{w_2}{\sqrt{2\pi}\sigma_2} e^{-\frac{(x-\mu_2)^2}{2\sigma_2^2}}\right],$$

$$x \in [0,1], \tag{19}$$

where $w_1 + w_2 = 1$.

2) *ORIS 2*: MLE-AIC selects a truncated Weibull model:

$$f_{\cos\varphi_2}(x) = \frac{1}{Z_2}\frac{k_w}{\lambda_w}\left(\frac{x - x_{\min}}{\lambda_w}\right)^{k_w - 1} e^{-\left(\frac{x - x_{\min}}{\lambda_w}\right)^{k_w}},$$

$$x \in [0,1]. \tag{20}$$

3) *ORIS 3*: MLE-AIC selects a truncated double-Gaussian model:

$$f_{\cos\varphi_3}(x)=\frac{1}{Z_3}\left[\frac{w_3}{\sqrt{2\pi}\sigma_3}e^{-\frac{(x-\mu_3)^2}{2\sigma_3^2}}+\frac{w_4}{\sqrt{2\pi}\sigma_4}e^{-\frac{(x-\mu_4)^2}{2\sigma_4^2}}\right],$$

$$x\in[0,1], \tag{21}$$

where $w_3+w_4=1$.

4) *ORIS 4*: MLE-AIC selects a truncated Rayleigh model:

$$f_{\cos\varphi_4}(x)=\frac{1}{Z_4}\frac{x}{\sigma_r^2}\exp\left(-\frac{x^2}{2\sigma_r^2}\right),\quad x\in[0,1]. \tag{22}$$

For an in-FoV sample, $H_k = K_{\text{path},k}X_k$. The conditional channel-gain density therefore follows by a standard change of variables:

$$f_{H_k|H_k>0}(h)=\frac{f_{X_k}(h/K_{\text{path},k})}{K_{\text{path},k}\Pr(X_k\geq\cos\psi_c)},$$

$$h\in[K_{\text{path},k}\cos\psi_c, K_{\text{path},k}], \tag{23}$$

and the outage probability is retained as a point mass at zero:

$$\Pr(H_k=0)=\Pr(X_k<\cos\psi_c). \tag{24}$$

Figure 2 compares the fitted continuous densities with the available Monte Carlo histograms. Panels (a) and (c) show the incidence-cosine fits, and panels (b) and (d) show the corresponding positive channel-gain distributions. FoV outages are handled separately through the zero-gain mass in Eq. (24).

The assumed receiver and ORIS control architecture is consistent with practical bandwidth constraints. Side-facing photodetectors can be integrated along the device frame [17], while MEMS micromirrors typically reconfigure within 0.1–1 ms [12], shorter than representative sitting-user posture-coherence times ($\sim$ 50 ms [9]). Updating $q_{i,n,j}$ at the statistical-CSI scale (e.g., every $\sim$ 100 ms) is therefore a reasonable assumption for tracking slow mean-orientation variations. LED scheduling and ORIS control are assumed to be synchronized; timing mismatch is outside the scope of the present model.

The model remains a statistical-CSI resource-allocation framework rather than a hardware prototype. For non-target users, residual ORIS leakage is evaluated by the same Lambertian propagation model, giving a conservative spill-over estimate. In practice, mirror misalignment, insertion loss, finite switching latency, calibration errors, and PDF-estimation errors would reduce the reflected gain; these effects can be represented by lowering ρ, increasing the uncertainty of $\hat{h}_{i,u,j}$, or adding bounded pointing loss to $H^{\text{ORIS}}_{i,n,j}$. The sensitivity tests in Section 5 therefore report performance under reduced ρ, different FoV values, and larger orientation variance.

2.3. Received Signal and Signal to Interference and Noise Ratio (SINR)

The fundamental VLC links adhere to the Lambertian radiation paradigm. The line-of-sight (LoS) channel gain between LED i and user j relies strictly on their spatial geometry:

$$H^{\text{LoS}}_{i,j} = \frac{(m+1)A_{PD}}{2\pi d_{i,j}^2}\cos^m(\phi_{i,j})T_s g\cos(\varphi_{i,j})\mathbb{I}$$

$$\{0\leq\varphi_{i,j}\leq\psi_c\} \tag{25}$$

where $m = -\ln 2/\ln\cos\Phi_{1/2}$ represents the Lambertian emission index parameterized by the LED semi-angle at half-power $\Phi_{1/2}$, and A_{PD} is the physical detector area equipped with optical-filter gain T_s and concentrator gain g. The parameter $d_{i,j}$ marks the Euclidean LoS distance. Crucially, $\phi_{i,j}$ denotes the irradiation angle emitted from the LED bore-sight, and $\varphi_{i,j}$ signifies the incidence angle measured relative to the active-PD normal vector, tightly constrained by the receiver field-of-view (FoV) threshold ψ_c.

Conversely, the non-line-of-sight (NLoS) branches rely on ORIS specular micromirrors executing Snell's law reflections [19]. The effective cascaded NLoS gain reflected via the n-th ORIS unit is derived as:

$$H^{\text{ORIS}}_{i,n,j} = \rho\frac{(m+1)A_{PD}}{2\pi(d_{i,n}+d_{n,j})^2}\cos^m(\phi_{i,n})T_s g\cos(\varphi_{n,j})$$

$$\times\mathbb{I}\{0\leq\varphi_{n,j}\leq\psi_c\} \tag{26}$$

encompassing the LED-to-mirror irradiation angle $\phi_{i,n}$, the intrinsic optical specular reflection coefficient $\rho\in(0,1]$, and the incidence angle $\varphi_{n,j}$ at the PD corresponding to the n-th ORIS unit. The composite free-space path loss cascades over the serially expanded propagation distances $d_{i,n}$ and $d_{n,j}$. The total superimposed composite channel aggregates as:

$$H_{i,j}=H^{\text{LoS}}_{i,j}+\sum_{n=1}^{N}q_{i,n,j}H^{\text{ORIS}}_{i,n,j} \tag{27}$$

The binary variable $f_{i,j}$ indicates whether LED i serves user j. It is optimized jointly with power and ORIS activation rather than fixed by a maximum-channel heuristic.

$$f_{i,j}=\begin{cases}1, & \text{if } i\text{th LED serves } j\text{th user}\\ 0, & \text{otherwise}\end{cases} \tag{28}$$

$$q_{i,n,j}=\begin{cases}1, & \text{if } n\text{th ORIS serves } j\text{th user via LED } i\\ 0, & \text{otherwise}\end{cases} \tag{29}$$

We use an equivalent baseband intensity-modulation/direct-detection (IM/DD) model. The variable $p_{i,j}\geq 0$ is the optical modulation amplitude allocated by LED i to user j, measured in watts. The Lambertian gains H^{LoS} and H^{ORIS} are dimensionless, and R_{PD} (A/W) denotes the photodetector responsivity. Define the effective optical channel and its electrical-domain counterpart as

$$H_{i,u,j} \triangleq H^{\text{LoS}}_{i,j}+\sum_{n=1}^{N}q_{i,n,u}H^{\text{ORIS}}_{i,n,j},$$

$$\widetilde{H}_{i,u,j} \triangleq R_{\text{PD}}H_{i,u,j}, \tag{30}$$

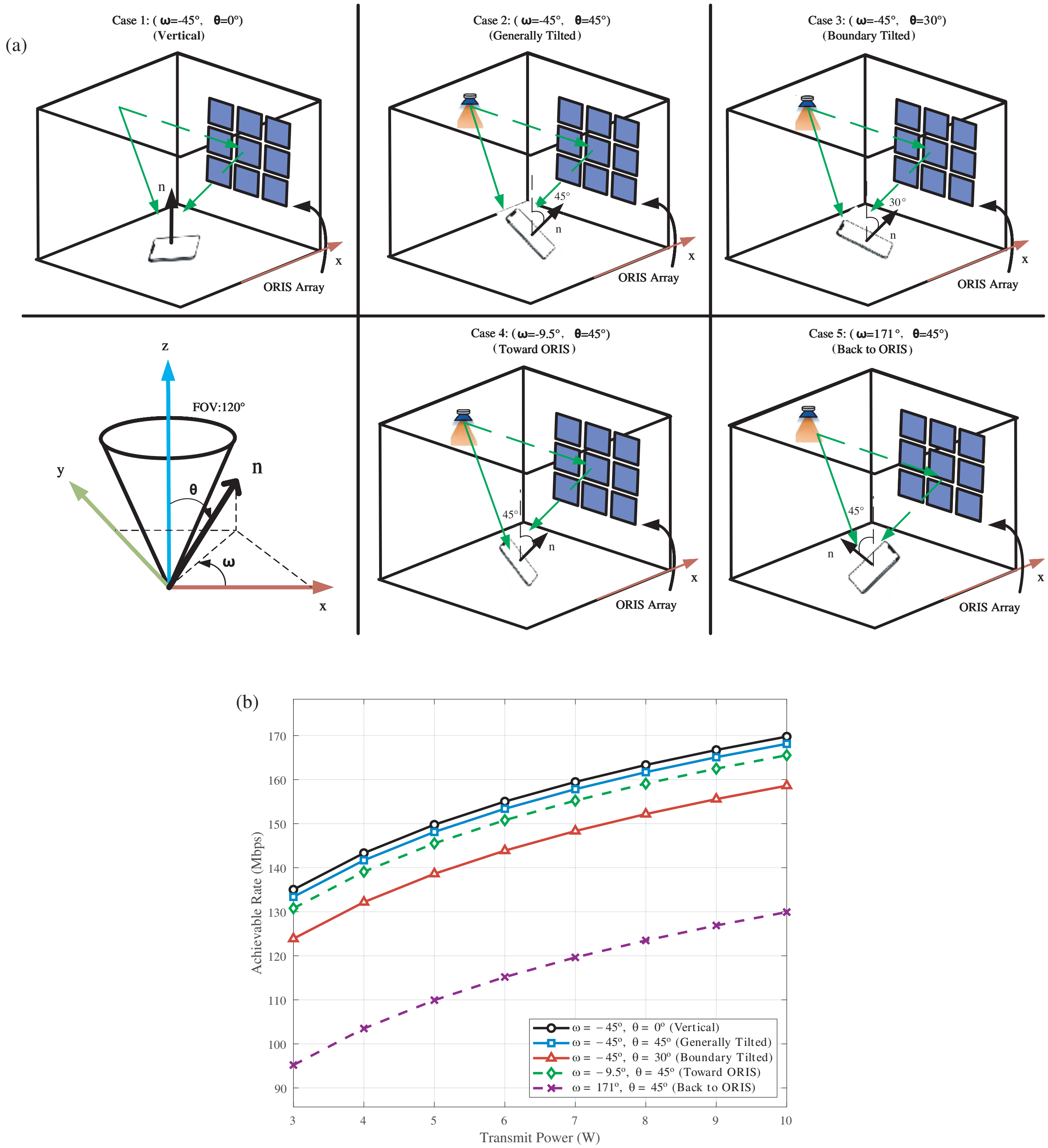

FIGURE 3. Single-user orientation-sensitivity experiment. (a) Representative orientation cases; the azimuth label ω inside the legacy panel corresponds to ζ in the text. (b) Shannon rate versus optical transmit power.

Here, u identifies the data stream and its ORIS pattern, and j identifies the receiving user. The direct path is independent of u. The statistical electrical-channel moment used by the optimizer is $\hat{h}_{i,u,j} \triangleq \mathbb{E}[|\widetilde{H}_{i,u,j}|^2]$. It is evaluated from the original Euler-angle samples with the FoV gates in Eqs. (25) and (26).

Let $\mathscr{J}_i \triangleq \{j : f_{i,j} = 1\}$ be the NOMA user set of LED i. Because ORIS activation changes $\hat{h}_{i,j,j}$, the SIC order is recomputed after each ORIS update by sorting $\{\hat{=}h_{i,j,j}\}_{j\in\mathscr{J}_i}$ in ascending order. Thus, $\pi_i(j_1) < \pi_i(j_2)$ if $\hat{h}_{i,j_1,j_1} < \hat{h}_{i,j_2,j_2}$.

User j cancels streams u with $\pi_i(u) < \pi_i(j)$ and treats streams with $\pi_i(u) > \pi_i(j)$ as residual interference. The transmitted data streams are mutually independent and normalized to unit second moment, so cross-products vanish after time averaging. Electrical signal and interference powers therefore add as sums of $|\widetilde{H}p|^2$:

$$S_j = \sum_{i\in\mathscr{I}} f_{i,j} \left|\widetilde{H}_{i,j,j}\, p_{i,j}\right|^2, \qquad (31)$$

$$
\begin{aligned}
I_j \; &= \underbrace{\sum_{u\in\mathscr{J}_{i_j^\star},\,\pi_{i_j^\star}(u)>\pi_{i_j^\star}(j)} \left|\widetilde{H}_{i_j^\star,u,j}\, p_{i_j^\star,u}\right|^2}_{I_j^{\text{intra}}\text{: SIC-residual co-LED interference}} \\
&\quad + \underbrace{\sum_{i\in\mathscr{I},\,i\neq i_j^\star}\sum_{u\in\mathscr{J}} f_{i,u}\left|\widetilde{H}_{i,u,j}\, p_{i,u}\right|^2}_{I_j^{\text{inter}}\text{: cross-LED interference}}, \qquad (32)
\end{aligned}
$$

$$
\mathrm{SINR}_j \; = \; \frac{S_j}{I_j+\sigma^2}. \qquad (33)
$$

Here, $i_j^\star \triangleq \arg\max_i f_{i,j}$ is well defined because each user is associated with exactly one LED, and σ^2 is the aggregate electrical noise variance in A^2. Accordingly, S_j, I_j, and σ^2 all have units A^2.

For modulation bandwidth B and Euler's number e, the achievable IM/DD rate is lower-bounded by [5, 19]

$$
R_j \geq \tfrac{B}{2}\log_2\left(1+\tfrac{e}{2\pi}\cdot \mathrm{SINR}_j\right), \qquad (34)
$$

in which the prefactor $\frac{1}{2}$ stems from the real-valued IM/DD baseband characteristics, and $e/(2\pi)$ represents the capacity penalty induced by the non-negativity constraint on emitted intensity. Hereafter, R_j strictly denotes the lower bound in Eq. (34) as the effective operating rate.

2.4. Orientation-Induced Rate Fluctuation

To theoretically motivate the necessity of ORIS-assisted orientation compensation, the channel fading effects induced exclusively by random user rotation are isolated via a minimal single-user configuration, absent multi-user networking, and resource association complexities. This conceptual setup integrates a single ceiling LED at $(2.5, 2.5, 3)$ m, one $2\,\mathrm{m}\times 2\,\mathrm{m}$ ORIS array mounted on the right wall at $(5, 2.5, 1.5)$ m, and one test user situated at $(2.0, 3.0, 1.0)$ m. For visual clarity and to prevent premature scale suppression by the IM/DD mapping factor (≈ 0.43), the standard Shannon rate $R_{\text{sgl}} = B\log_2(1+\text{SNR})$ is temporarily used as the pure illustrative capacity metric.

Figure 3 compares representative orientations relative to one active ORIS. At 10 W, the simulation plot reports about 124 Mbps when the side PD points away from the ORIS and 165 Mbps when it points toward the ORIS. This example motivates orientation-aware resource allocation; it is not used as the multi-user objective or as evidence for arbitrary rotations.

3. PROBLEM FORMULATION

3.1. Statistical-CSI Surrogate Objective via Jensen Bound

For an illustrative single link, let p be a fixed optical modulation amplitude and $\widetilde{H} = R_{\text{PD}}H$ be the random electrical-domain channel. The exact ergodic rate requires integration over (α,β,γ). Concavity of $\log_2(1+x)$ gives

$$
\begin{aligned}
\mathbb{E}_{\widetilde{H}}[R] \; &= \; \mathbb{E}\left[\tfrac{B}{2}\log_2\left(1+\kappa\tfrac{p^2|\widetilde{H}|^2}{\sigma^2}\right)\right] \\
&\leq \tfrac{B}{2}\log_2\left(1+\kappa\tfrac{p^2\,\mathbb{E}[|\widetilde{H}|^2]}{\sigma^2}\right) \triangleq R^{\text{UB}},
\end{aligned}
$$

TABLE 2. Monte-Carlo validation of the Jensen surrogate. Entries are relative gaps $100(R^{\text{UB}}-\mathbb{E}[R])/\mathbb{E}[R]$ in percent.

Average SNR	$\sigma_\theta = 5^\circ$	$\sigma_\theta = 10^\circ$	$\sigma_\theta = 15^\circ$
25 dB	0.22	0.75	1.65
35 dB	0.15	0.52	1.17
45 dB	0.11	0.40	0.89

$$
\kappa \triangleq \frac{e}{2\pi}. \qquad (35)
$$

Let $Z \triangleq |\widetilde{H}|^2$, $a \triangleq \kappa p^2/\sigma^2$, and $\mu_Z \triangleq \mathbb{E}[Z]$. The Jensen gap is

$$
\Delta_J \triangleq \tfrac{B}{2}\log_2(1+a\mu_Z) - \mathbb{E}\left[\tfrac{B}{2}\log_2(1+aZ)\right] \geq 0. \qquad (36)
$$

Since $g(z) = \frac{B}{2}\log_2(1+az)$ satisfies $g''(z) = -\frac{B}{2\ln 2}\frac{a^2}{(1+az)^2}$, Taylor's theorem around μ_Z gives the bound

$$
0 \leq \Delta_J \leq \frac{B}{4\ln 2}\frac{a^2\mathrm{Var}(Z)}{(1+az_{\min})^2} \leq \frac{B}{4\ln 2}a^2\mathrm{Var}(Z), \qquad (37)
$$

where $z_{\min}$ is the lower support bound of Z. Thus, the single-link surrogate error is controlled by the dispersion of the electrical-channel power.

The bound depends on $\mathrm{Var}(Z)$, which requires the fourth-order channel moment $\mathbb{E}[|\widetilde{H}|^4]$ in addition to $\hat{h} \triangleq \mathbb{E}[|\widetilde{H}|^2]$. The following proposition states its limited role.

Proposition 1 *For a fixed optical modulation amplitude, Eq. (35) is an upper bound on the exact single-link ergodic IM/DD rate. The bound is a motivation for the statistical-CSI proxy; it is not an upper bound on the coupled multi-user rate in general.*

Proof: The statement follows from the concavity of $\log_2(1+x)$ for $x \geq 0$. The subsequent multi-user formulation uses a moment-matched approximation and therefore does not imply global optimality for the original stochastic MINLP.

Table 2 compares Eq. (35) with direct Monte Carlo evaluation using 10^6 channel samples. The average $\mathbb{E}[|\widetilde{H}|^2]$ is normalized at each SNR point to isolate the orientation-induced Jensen gap. The reported gap remains below 1.7% over the tested range and below 0.8% for $\sigma_\theta \leq 10^\circ$.

For the multi-user SINR, desired and interference powers are coupled through the same orientation. We therefore use the following moment-matched approximation, not a Jensen bound:

$$
\begin{aligned}
&\mathbb{E}\left[\tfrac{B}{2}\log_2\left(1+\frac{\kappa S_j}{I_j+\sigma^2}\right)\right] \\
&\approx \tfrac{B}{2}\log_2\left(1+\frac{\kappa\,\mathbb{E}[S_j]}{\mathbb{E}[I_j]+\sigma^2}\right), \quad \kappa = \frac{e}{2\pi}. \qquad (38)
\end{aligned}
$$

Define $\widehat{\mathrm{SINR}}_j$ and the corresponding surrogate rate $\bar{R}_j$ as follows:

$$
\widehat{\mathrm{SINR}}_j \;\triangleq\; \frac{\hat{h}_{i_j^\star,j,j}\,p_{i_j^\star,j}^2}{\widehat{I}_j(\mathbf{P})+\sigma^2}, \qquad \bar{R}_j \triangleq \frac{B}{2}\log_2\left(1+\kappa\widehat{\mathrm{SINR}}_j\right),
$$

$$\widehat{I}_j(\mathbf{P}) \triangleq \sum_{\substack{u\in\mathscr{J}_{i_j^\star}\\ \pi_{i_j^\star}(u)>\pi_{i_j^\star}(j)}} \hat{h}_{i_j^\star,u,j}\, p_{i_j^\star,u}^2 + \sum_{\substack{k\in\mathscr{I}\\ k\neq i_j^\star}} \sum_{u\in\mathscr{J}} f_{k,u}\,\hat{h}_{k,u,j}\,p_{k,u}^2, \tag{39}$$

where $\hat{h}_{i,u,j} = \mathbb{E}[|\widetilde{H}_{i,u,j}|^2]$. The numerator is the desired mean electrical signal power, and $\widehat{I}_j$ is the sum of residual mean electrical interference powers.

3.2. Joint Resource Allocation Problem

We maximize the weighted statistical-CSI surrogate sum rate. The non-negative coefficient ω_j is the priority weight of user j:

$$\begin{aligned}
(\mathscr{P}):\ \max_{\mathbf{P},\mathbf{F},\mathbf{Q}}\quad & \sum_{j\in\mathscr{J}} \omega_j \bar{R}_j \\
\text{s.t.}\quad & \text{C1: } \bar{R}_j = \tfrac{B}{2}\log_2\left(1+\kappa\widehat{\mathrm{SINR}}_j\right),\ \ \forall j\in\mathscr{J} \\
& \text{C2: } \bar{R}_j \geqslant R_{\min},\quad \forall j\in\mathscr{J} \\
& \text{C3(a): } 0\le p_{i,j}\le f_{i,j}P_{\max}^{\mathrm{opt}},\quad \forall i,j \\
& \text{C3(b): } \sum_{j\in\mathscr{J}} p_{i,j}\leqslant P_{\max}^{\mathrm{opt}},\quad \forall i \\
& \text{C4: } f_{i,j}\in\{0,1\},\ \ \forall i\in\mathscr{I},\ j\in\mathscr{J} \\
& \text{C5: } \sum_{i\in\mathscr{I}} f_{i,j}=1,\quad \forall j\in\mathscr{J} \\
& \text{C6: } \sum_{j\in\mathscr{J}} f_{i,j}\leqslant N_{\max},\quad \forall i\in\mathscr{I} \\
& \text{C7: } q_{i,n,j}\in\{0,1\},\ \ \forall i,n,j \\
& \text{C8: } \sum_{i\in\mathscr{I}}\sum_{j\in\mathscr{J}} q_{i,n,j}\leqslant 1,\ \ \forall n\in\mathscr{N} \\
& \text{C9: } q_{i,n,j}\le f_{i,j},\quad \forall i,n,j \\
& \text{C10: } p_{i,u}\ge p_{i,j},\quad \forall u,j\in\mathscr{J}_i:\ \pi_i(u)<\pi_i(j)
\end{aligned} \tag{40}$$

Constraint C1 defines the deterministic statistical-CSI surrogate rate, and C2 enforces the minimum QoS. Constraints C3(a)–C3(b) impose the optical-power budget and force unassociated powers to zero. Constraints C4–C6 define a unique LED association and the per-LED NOMA load. Constraints C7–C9 impose binary ORIS activation, per-unit exclusivity, and association consistency. Constraint C10 explicitly enforces the descending power order required by the adopted weakest-first SIC convention.

4. RESOURCE ALLOCATION ALGORITHM FOR ACHIEVABLE RATE MAXIMIZATION

Problem $(\mathscr{P})$ is a non-convex mixed-integer nonlinear programming (MINLP) formulation due to the strong coupling among the continuous power variables $\mathbf{P}$, binary association indicators $\mathbf{F}$, and discrete ORIS activation states $\mathbf{Q}$. Since obtaining a global optimum directly is computationally prohibitive, we develop an alternating optimization framework based on block coordinate descent (BCD).

4.1. Proposed BCD Framework

The BCD framework updates power $(\mathscr{P}_1)$, user association $(\mathscr{P}_2)$, and ORIS activation $(\mathscr{P}_3)$ in sequence. Each relaxed candidate is projected to the original feasible set and accepted only when it does not reduce $\sum_j \omega_j \bar{R}_j$.

After each $\mathbf{Q}$ update, the moments $\hat{h}_{i,j,j}$ and the ascending SIC order π_i are recomputed before the next $\mathscr{P}_1$ update. This allows the power allocation to track the statistical channel reshaping caused by ORIS activation.

Proposition 2 *Assume that each projected block update is feasible and is accepted only when it does not decrease $\sum_j \omega_j \bar{R}_j$. Then the objective sequence generated by Algorithm 1 converges to a finite value.*

Proof: The per-LED power constraints, finite user set, and finite ORIS activation set imply an upper-bounded achievable weighted sum rate for any fixed bandwidth and noise variance. By the acceptance rule, the objective value after each block update is non-decreasing. Hence, the generated scalar objective sequence is monotone and bounded above, and therefore converges. Because $\mathbf{F}$ and $\mathbf{Q}$ are recovered via relaxation and binary projection, this result should be interpreted as convergence to a feasible locally stable solution of the adopted surrogate problem, not as a guarantee of global optimality or stationarity for the original mixed-integer stochastic program.

4.2. Power Allocation via Fractional Programming $(\mathscr{P}_1)$

For fixed $\mathbf{F}$ and $\mathbf{Q}$, subproblem $\mathscr{P}_1$ optimizes the optical modulation amplitudes of active links. Powers of inactive links are fixed to zero. The statistical SIC order is also fixed within this block:

$$\begin{aligned}
\max_{\mathbf{P}\geq\mathbf{0}}\quad & \sum_{j\in\mathscr{J}} \omega_j \bar{R}_j \\
\text{s.t.}\quad & \sum_{j\in\mathscr{J}_i} p_{i,j}\leqslant P_{\max}^{\mathrm{opt}},\quad \forall i\in\mathscr{I}, \\
& p_{i,u}\ge p_{i,j},\quad \forall u,j\in\mathscr{J}_i:\ \pi_i(u)<\pi_i(j).
\end{aligned} \tag{41}$$

For compactness, denote the statistical residual interference in Eq. (39) by $\mathscr{I}_j(\mathbf{P})$:

$$\mathscr{I}_j(\mathbf{P}) \triangleq \sum_{\substack{u\in\mathscr{J}_{i_j^\star}\\ \pi_{i_j^\star}(u)>\pi_{i_j^\star}(j)}} \hat{h}_{i_j^\star,u,j}\, p_{i_j^\star,u}^2 + \sum_{\substack{k\in\mathscr{I}\\ k\neq i_j^\star}} \sum_{u\in\mathscr{J}} f_{k,u}\,\hat{h}_{k,u,j}\,p_{k,u}^2. \tag{42}$$

Algorithm 1 Proposed BCD Algorithm for Sum-Rate Maximization Problem (P)

Initialize: Outer-iteration index $t \leftarrow 0$, convergence tolerance ε, initial feasible solutions $\mathbf{Q}^{(0)}$, $\mathbf{F}^{(0)}$, and $\mathbf{P}^{(0)}$.
Output: Optimized activation tensor $\mathbf{Q}^*$ and matrices $\mathbf{F}^*$ and $\mathbf{P}^*$.
repeat
  Step 1 (Power Allocation): Given $\mathbf{F}^{(t)}$ and $\mathbf{Q}^{(t)}$, solve subproblem $(\mathscr{P}_1)$ to obtain $\mathbf{P}^{(t+1)}$.
  If the surrogate objective decreases, set $\mathbf{P}^{(t+1)} \leftarrow \mathbf{P}^{(t)}$.
  Step 2 (User Association): Given $\mathbf{P}^{(t+1)}$ and $\mathbf{Q}^{(t)}$, solve subproblem $(\mathscr{P}_2)$ to obtain $\mathbf{F}^{(t+1)}$.
  If the rounded association decreases the surrogate objective, set $\mathbf{F}^{(t+1)} \leftarrow \mathbf{F}^{(t)}$.
  Step 3 (ORIS Activation): Given $\mathbf{P}^{(t+1)}$ and $\mathbf{F}^{(t+1)}$, solve subproblem $(\mathscr{P}_3)$ to obtain $\mathbf{Q}^{(t+1)}$.
  If the recovered binary ORIS pattern decreases the surrogate objective, set $\mathbf{Q}^{(t+1)} \leftarrow \mathbf{Q}^{(t)}$.
  Calculate the surrogate objective $\bar{R}_{\text{sum}}^{(t+1)} = \sum_j \omega_j \bar{R}_j$.
  Update outer-iteration index $t \leftarrow t+1$.
Until $|\bar{R}_{\text{sum}}^{(t)} - \bar{R}_{\text{sum}}^{(t-1)}| \le \varepsilon$
Return $\mathbf{Q}^* \leftarrow \mathbf{Q}^{(t)}$, $\mathbf{F}^* \leftarrow \mathbf{F}^{(t)}$, $\mathbf{P}^* \leftarrow \mathbf{P}^{(t)}$.

Introduce a non-negative multiplier λ_i for each per-LED budget:

$$\mathscr{L}(\mathbf{P}, \boldsymbol{\lambda}) = \sum_{j \in \mathscr{J}} \omega_j \bar{R}_j - \sum_{i \in \mathscr{I}} \lambda_i \left(\sum_{j \in \mathscr{J}_i} p_{i,j} - P_{\max}^{\text{opt}} \right). \quad (43)$$

Define $\widetilde{\omega}_j \triangleq \omega_j B/(2\ln 2)$ and $\kappa = e/(2\pi)$. Using natural logarithms, the Lagrangian dual transform with auxiliary variables $\boldsymbol{\Gamma}$ is [14]

$$\mathcal{L}_{\text{FP}}(\mathbf{P}, \boldsymbol{\Gamma}, \boldsymbol{\lambda}) = \sum_{j \in \mathcal{J}} \widetilde{\omega}_j \left[\ln(1+\Gamma_j) - \Gamma_j + \frac{(1+\Gamma_j)\kappa \hat{h}_{i_j^\star,j,j} p_{i_j^\star,j}^2}{\kappa \hat{h}_{i_j^\star,j,j} p_{i_j^\star,j}^2 + \mathcal{I}_j(\mathbf{P}) + \sigma^2} \right] - \sum_{i \in \mathcal{I}} \lambda_i \left(\sum_{j \in \mathcal{J}_i} p_{i,j} - P_{\max}^{\text{opt}} \right). \quad (44)$$

Applying the quadratic transform introduces real auxiliary variables y_j:

$$\begin{aligned}\mathscr{L}_{\text{QT}}(\mathbf{P}, \boldsymbol{\Gamma}, \mathbf{y}, \boldsymbol{\lambda}) = \sum_{j \in \mathscr{J}} \widetilde{\omega}_j \Big[&\ln(1+\Gamma_j) - \Gamma_j + 2y_j \sqrt{\kappa(1+\Gamma_j)\hat{h}_{i_j^\star,j,j}}\, p_{i_j^\star,j} \\ &- y_j^2 \left(\kappa \hat{h}_{i_j^\star,j,j} p_{i_j^\star,j}^2 + \mathscr{I}_j(\mathbf{P}) + \sigma^2 \right) \Big] \\ &- \sum_{i \in \mathscr{I}} \lambda_i \left(\sum_{j \in \mathscr{J}_i} p_{i,j} - P_{\max}^{\text{opt}} \right), \end{aligned} \quad (45)$$

rendering the objective conditionally concave-quadratic with respect to $p_{i,j}$.

For fixed $\mathbf{P}$, the exact auxiliary updates are

$$\Gamma_j^{(t+1)} = \frac{\kappa\, \hat{h}_{i_j^\star,j,j}\, (p_{i_j^\star,j}^{(t)})^2}{\mathscr{I}_j(\mathbf{P}^{(t)}) + \sigma^2}, \quad (46)$$

Algorithm 2 FP-Lagrangian NOMA Power Allocation with Dynamic SIC $(\mathscr{P}_1)$

Input: Fixed $\mathbf{F}$, $\mathbf{Q}$, warm-start $\mathbf{P}^{(0)}$, optical-power budget $P_{\max}^{\text{opt}}$, bisection bound $\Lambda_{\max}$, tolerances $\varepsilon_p, \varepsilon_\lambda$, and iteration cap $T_{\max}$.
Output: Updated optical-power matrix $\mathbf{P}^\star$.
Initialize $\mathbf{P}^{(0)}$ from the previous BCD iterate or by equal splitting over each $\mathscr{J}_i$.
SIC ordering: Sort $\{\hat{h}_{i,j,j}\}_{j \in \mathscr{J}_i}$ in ascending order for every LED i.
Initialize $\boldsymbol{\Gamma}^{(0)}$ via Eq. (46); $t \leftarrow 0$.
repeat
  Step 1 ($\boldsymbol{\Gamma}$-update): Update $\Gamma_j^{(t+1)}$ via Eq. (46).
  Step 2 ($\mathbf{y}$-update): For each j, compute $y_j^{(t+1)}$ via Eq. (47).
  Step 3 ($\mathbf{P}$-update):
    Compute $\{\alpha_{i,j}, \beta_{i,j}\}$ for active links.
    Set $\lambda_i = 0$ if $g_i(0) \le P_{\max}^{\text{opt}}$; otherwise find the root in Eq. (51) by bisection.
    Form $\widetilde{\mathbf{p}}_i$ using Eq. (50) and project it onto $\mathscr{C}_i$ by bounded isotonic regression.
  $t \leftarrow t+1$.
until $\|\mathbf{P}^{(t)} - \mathbf{P}^{(t-1)}\|_F \,/\, \|\mathbf{P}^{(t-1)}\|_F \le \varepsilon_p$ **or** $t \ge T_{\max}$.
Return $\mathbf{P}^\star \leftarrow \mathbf{P}^{(t)}$.

$$y_j^{(t+1)} = \frac{\sqrt{\kappa(1+\Gamma_j^{(t+1)})\hat{h}_{i_j^\star,j,j}}\; p_{i_j^\star,j}^{(t)}}{\kappa\, \hat{h}_{i_j^\star,j,j}\, (p_{i_j^\star,j}^{(t)})^2 + \mathscr{I}_j(\mathbf{P}^{(t)}) + \sigma^2}. \quad (47)$$

For fixed $(\boldsymbol{\Gamma}, \mathbf{y})$, each active-link term is $2\alpha_{i,j} p_{i,j} - \beta_{i,j} p_{i,j}^2$, where

$$\alpha_{i,j} \triangleq \widetilde{\omega}_j \sqrt{\kappa(1+\Gamma_j)\hat{h}_{i,j,j}}\, y_j, \quad j \in \mathscr{J}_i, \quad (48)$$

$$\beta_{i,j} \triangleq \widetilde{\omega}_j y_j^2 \kappa \hat{h}_{i,j,j} + \sum_{\substack{v \in \mathscr{J}_i \\ \pi_i(v) < \pi_i(j)}} \widetilde{\omega}_v y_v^2 \hat{h}_{i,j,v} + \sum_{\substack{v \in \mathscr{J} \\ i_v^\star \neq i}} \widetilde{\omega}_v y_v^2 \hat{h}_{i,j,v}, \quad j \in \mathscr{J}_i. \quad (49)$$

The three terms account for the intended stream, residual co-LED interference, and cross-LED interference, respectively. Inactive links are excluded from $\mathscr{J}_i$ and fixed to zero, avoiding undefined $0/0$ updates.

Ignoring C10 momentarily, Karush–Kuhn–Tucker (KKT) stationarity gives the active-link candidate

$$\widetilde{p}_{i,j}(\lambda_i) = \begin{cases} \left[\dfrac{2\alpha_{i,j} - \lambda_i}{2\beta_{i,j}} \right]_0^{P_{\max}^{\text{opt}}}, & \beta_{i,j} > 0, \\ 0, & \beta_{i,j} = 0, \end{cases} \quad (50)$$

where $[x]_a^b = \min(\max(x,a),b)$. Let $g_i(\lambda_i) = \sum_{j \in \mathscr{J}_i} \widetilde{p}_{i,j}(\lambda_i)$. The multiplier is

$$\lambda_i^\star = \begin{cases} 0, & g_i(0) \le P_{\max}^{\text{opt}}, \\ \text{the root of } g_i(\lambda_i) = P_{\max}^{\text{opt}}, & g_i(0) > P_{\max}^{\text{opt}}, \end{cases} \quad (51)$$

Algorithm 3 SDR-based ORIS Sparse Activation ($\mathscr{P}_3$)

```
Input: Fixed P, F, current Q^(t), and M_rand randomization trials.
Output: Updated Q^(t+1).
Lift: Form Y = [X, q; q^T, 1], impose Eq. (54), and drop rank(Y) = 1.
Use Eq. (53) to construct a concave lower surrogate of the rate.
Solve the SDP to obtain (q*, X*, Y*).
if rank(Y*) = 1
    Threshold the last column and project it onto C8–C9.
else
    Draw M_rand samples from N(q*, X* − q*(q*)^T).
    Threshold and project every sample onto C8–C9.
    Select the feasible candidate with the largest original surrogate objective.
end if
Return Q^(t+1).
```

The root is found by bisection because g_i is non-increasing. After this budget update, the vector is projected onto the convex ordered simplex

$$\mathscr{C}_i = \{\mathbf{p}_i:\ p_{i,u} \geq p_{i,j} \text{ if } \pi_i(u) < \pi_i(j),\ \mathbf{p}_i \geq 0,\ \mathbf{1}^T\mathbf{p}_i \leq P_{\max}^{\text{opt}}\}$$

using bounded isotonic regression. The projected candidate is accepted only if it is feasible and does not reduce the outer surrogate objective. This explicitly enforces C10; no claim is made that the descending NOMA power profile emerges automatically.

4.3. User Association Optimization ($\mathscr{P}_2$)

For fixed $\mathbf{P}$ and $\mathbf{Q}$, optimizing the user association matrix $\mathbf{F}$ constitutes an intractable integer nonlinear programming (INLP) subproblem owing to the fractional-logarithmic coupling of binary indicators. This intractability is bypassed via successive convex approximation (SCA). First, the Boolean domain $\{0, 1\}$ is relaxed into the continuous boundary $[0, 1]$. A tractable convex surrogate is then iteratively constructed utilizing a first-order Taylor expansion evaluated at the preceding iterate.

After SCA convergence, the relaxed matrix is projected to a binary assignment satisfying C5 and C6. Because $\mathbf{Q}$ is fixed in this block, any pair with $q_{i,n,j} = 1$ is assigned with $f_{i,j} = 1$ to preserve C9. The projected candidate is then checked against C2 and the outer acceptance rule.

4.4. ORIS Sparse Activation Optimization ($\mathscr{P}_3$)

Let $M \triangleq INJ$ and stack the activation tensor into $\mathbf{q} \in \{0, 1\}^M$. With $\mathbf{P}$ and $\mathbf{F}$ fixed, $\mathscr{P}_3$ is a binary QCQP subject to C8 and C9.

The statistical desired and interference powers can be written as quadratic forms in $\mathbf{q}$:

$$\widehat{S}_j = \mathbf{q}^T\mathbf{A}_j\mathbf{q} + \mathbf{b}_j^T\mathbf{q} + c_j^S, \quad \widehat{I}_j = \mathbf{q}^T\mathbf{C}_j\mathbf{q} + \mathbf{d}_j^T\mathbf{q} + c_j^I, \quad (52)$$

Algorithm 4 SCA-based User Association Optimization ($\mathscr{P}_2$)

```
Input: Fixed P, Q, current F^(t), tolerance ε_f.
Output: Updated F^(t+1).
Relaxation: Relax binary variables f_{i,j} ∈ {0,1} to continuous boundaries f_{i,j} ∈ [0,1].
Initialize F_relax with F^(t).
repeat
    Construct a convex surrogate function via first-order Taylor expansion at F_relax.
    Solve the approximated convex problem using CVX to update F_relax.
until ||F_relax^new − F_relax^old||_F ≤ ε_f
Rounding: Recover a binary F^(t+1) satisfying C5, C6, and the fixed-Q coupling C9.
Return F^(t+1).
```

The matrices contain ORIS-reflected moment products; the vectors contain LoS-ORIS cross terms; and c_j^S, c_j^I contain LoS-only terms.

After lifting, $\widehat{I}_j$ is affine in the lifted variables. Because $-\log_2 z$ is convex, its tangent at $\widehat{I}_j^{(r)} + \sigma^2$ is a global lower bound:

$$-\log_2\left(\widehat{I}_j + \sigma^2\right) \geq -\log_2\left(\widehat{I}_j^{(r)} + \sigma^2\right) - \frac{\widehat{I}_j - \widehat{I}_j^{(r)}}{(\widehat{I}_j^{(r)} + \sigma^2)\ln 2}. \quad (53)$$

Use the exact augmented lifting $\mathbf{Y} = [\mathbf{q}^T, 1]^T[\mathbf{q}^T, 1]$, with $\mathbf{X} = \mathbf{Y}_{1:M,1:M}$ and $\mathbf{q} = \mathbf{Y}_{1:M,M+1}$. Dropping only $\text{rank}(\mathbf{Y}) = 1$ gives the SDP

$$\begin{aligned}
\max_{\mathbf{q},\mathbf{X},\mathbf{Y}} \quad & \sum_{j\in\mathscr{J}} \omega_j \widehat{R}_j^{(r)}(\mathbf{q}, \mathbf{X}) \\
\text{s.t.} \quad & \mathbf{Y} = \begin{bmatrix} \mathbf{X} & \mathbf{q} \\ \mathbf{q}^T & 1 \end{bmatrix} \succeq 0, \quad \text{diag}(\mathbf{X}) = \mathbf{q}, \\
& 0 \leq \mathbf{q} \leq 1, \quad \sum_{i\in\mathscr{I}}\sum_{j\in\mathscr{J}} q_{i,n,j} \leq 1, \quad \forall n \in \mathscr{N}, \\
& q_{i,n,j} \leq f_{i,j}, \quad \forall i, n, j,
\end{aligned} \quad (54)$$

where $\widehat{R}_j^{(r)}$ combines the concave first logarithm with the lower bound in Eq. (53). The exact lifting additionally requires $\text{rank}(\mathbf{Y}) = 1$; this is the sole dropped constraint.

If $\mathbf{Y}^\star$ is numerically rank one, its last column gives the relaxed activation vector, which is thresholded and projected onto C8–C9. Otherwise, define $\boldsymbol{\mu}_q = \mathbf{q}^\star$ and $\boldsymbol{\Sigma}_q = \mathbf{X}^\star - \mathbf{q}^\star(\mathbf{q}^\star)^T \succeq 0$. Draw M_{rand} samples from $\mathscr{N}(\boldsymbol{\mu}_q, \boldsymbol{\Sigma}_q)$, threshold them, and project each one by retaining at most one associated (i, j) pair per ORIS unit. The feasible candidate with the largest original surrogate objective is returned.

4.5. Computational Complexity Analysis

Let T_{BCD}, T_{FP}, T_{SCA}, and T_{SDR} denote the iteration counts of the four loops, and let M_{rand} be the number of Gaussian candidates. Here, N is the total number of ORIS units across all four walls.

TABLE 3. Simulation parameters.

Symbol	Description	Value
$D_x \times D_y \times D_z$	Room dimensions (m)	$5 \times 5 \times 3$
I, J	Number of LEDs/users	$4,\ 8$
N	Total ORIS units across four walls	36–100
$\Phi_{1/2}$	LED semi-angle at half power	60°
m	Lambertian order $(-\ln 2/\ln\cos\Phi_{1/2})$	1
A_{PD}	Photodetector physical area	$1\,\mathrm{cm}^2$
ψ_c	Receiver field-of-view (FoV)	60°
T_s, g	Optical filter & concentrator gains	$1.0,\ 1.5$
ρ	ORIS reflection coefficient	0.95
R_{PD}	PD responsivity	Absorbed in SNR normalization
$P_{\text{max}}^{\text{opt}}$	Maximum optical modulation budget	10 W
σ^2	Aggregate electrical noise variance	$10^{-21}\,\mathrm{A}^2$
B	Modulation bandwidth	20 MHz
R_{min}	Minimum per-user QoS rate	5 Mbps
μ_θ, b_θ	Polar-angle Laplace mean/scale	$29.7^\circ, 5.6^\circ$
$(\theta_{\text{min}}, \theta_{\text{max}})$	Polar-angle support	$(0^\circ, 90^\circ)$
$\bar{\boldsymbol{\xi}}$	Nominal Euler posture	Calibrated to μ_θ
$\sigma_{\delta\alpha,\delta\beta,\delta\gamma}$	Euler perturbation std-dev	5°
N_{max}	Max users per LED	4
$\varepsilon, \varepsilon_p, \varepsilon_f$	Convergence tolerances	10^{-3}
$T_{\text{BCD}}, T_{\text{SCA}}, T_{\text{FP}}$	Outer/inner iteration caps	$30,\ 20,\ 15$
M_{rand}	Gaussian-randomization candidates	200
N_{MC}	Monte-Carlo samples for PDF/gap validation	10^6
Seed	Random seed for reported stress tests	2026

1) *Power allocation*: Updating Γ_j, y_j, the bisection variables, and the ordered-simplex projection costs $\mathcal{O}(IJ + I\log(1/\varepsilon_\lambda))$ per FP iteration.

2) *User Association ($\mathcal{P}_2$)*: The continuous SCA convex approximation involves IJ relaxed variables. Employing standard interior-point methods, solving one convexified surrogate program demands a worst-case complexity of $\mathcal{O}((IJ)^{3.5})$, giving $\mathcal{O}(T_{\text{SCA}}(IJ)^{3.5})$ for this block.

3) *ORIS activation*: The augmented matrix $\mathbf{Y}$ has dimension $(INJ+1)\times(INJ+1)$. The asymptotic SDP cost remains $\mathcal{O}((INJ)^{4.5})$, and randomization adds $\mathcal{O}(M_{\text{rand}}(INJ)^2)$.

Consequently, the aggregate computational complexity is conservatively bounded by

$$\mathcal{O}_{\text{total}} = \mathcal{O}\Big(T_{\text{BCD}}\big[T_{\text{FP}}(IJ + I\log\varepsilon_\lambda^{-1}) + T_{\text{SCA}}(IJ)^{3.5} + T_{\text{SDR}}(INJ)^{4.5} + M_{\text{rand}}(INJ)^2\big]\Big). \tag{55}$$

With the simulation caps in Table 3, the algorithm typically converges within five outer BCD iterations. The SDR block is still the dominant cost and limits high-frequency real-time re-optimization. In practice, the method is best interpreted as a statistical-CSI/offline template optimizer that is recomputed when user distributions or room geometry change, while lightweight greedy ORIS updates can be used between full optimizations.

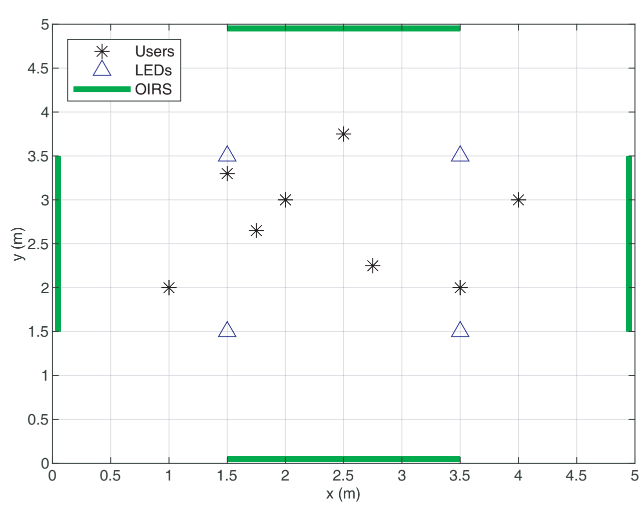

FIGURE 4. Schematic top view of the indoor VLC system topology, illustrating the coordinates of LED transmitters, user terminals, and ORIS modules.

TABLE 4. MLE parameters of the fitted truncated PDFs (cosine of incident angle).

Link	Distribution	Parameters	Numerical value
LoS	Trunc. Laplace	$(\mu_{\cos\varphi}, \lvert\ell_\theta\rvert b_\theta)$	$(0.832,\ 0.046)$
ORIS$_1$	Trunc. double Gaussian	(w_1, μ_1, σ_1)	$(0.62,\ 0.71,\ 0.08)$
		(w_2, μ_2, σ_2)	$(0.38,\ 0.34,\ 0.12)$
ORIS$_2$	Trunc. Weibull	$(k_w, \lambda_w, x_{\min})$	$(2.41,\ 0.32,\ 0.10)$
ORIS$_3$	Trunc. double Gaussian	(w_3, μ_3, σ_3)	$(0.55,\ 0.66,\ 0.09)$
		(w_4, μ_4, σ_4)	$(0.45,\ 0.29,\ 0.13)$
ORIS$_4$	Trunc. Rayleigh	σ_r	0.41

Notes: Continuous-density parameters obtained from the 10^6-sample MLE/AIC fits. FoV-outage samples contribute zero gain when evaluating channel moments.

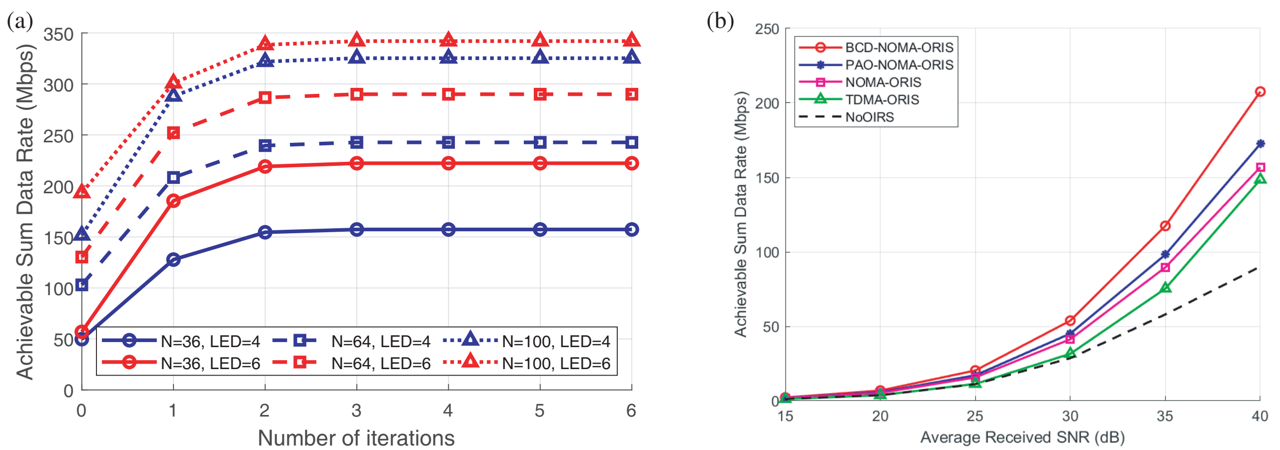

FIGURE 5. Simulation results of the proposed BCD algorithm for sum-rate maximization. (a) The convergence of the proposed BCD algorithm under different conditions regarding the number of LED and ORIS units and (b) the maximum achievable sum rate against escalating average received SNR constraints relative to standard baseline protocols.

5. SIMULATION RESULTS

To validate the proposed joint resource allocation framework, numerical evaluations are conducted in a standard $5 \times 5 \times 3\,\mathrm{m}^3$ indoor VLC downlink scenario with a receiving plane configured at a height of 1 m. The system nodal topology is depicted in Fig. 4. Four downward-facing LEDs act as optical base stations and are mounted to the ceiling in a symmetric 2×2 array at planar coordinates $(1.5, 1.5)$, $(3.5, 1.5)$, $(1.5, 3.5)$, and $(3.5, 3.5)$ m to guarantee illumination uniformity. The network serves $J = 8$ spatially multiplexed mobile terminals randomly distributed across the receiving plane, with representative test coordinates clustered at $(0.8, 1.9)$, $(1.5, 3.3)$, $(1.8, 2.7)$, $(2.0, 3.0)$, $(2.5, 3.4)$, $(2.8, 2.2)$, $(3.5, 2.1)$, and $(4.0, 3.0)$ m.

Four 2 m ORIS arrays are mounted on the four walls, and the total of N reflecting units is distributed across these arrays. Tables 3 and 4 list the simulation parameters and continuous-density fits. The orientation model is calibrated from [9, 10]. PDF fitting and Jensen-gap evaluation use 10^6 samples and seed 2026. No hardware experiment is claimed.

5.1. Convergence and Parameter Sensitivity Analysis

Figure 5(a) shows the convergence traces. In the tested configurations, the accepted surrogate objective increases rapidly during the first three iterations and changes little after about five iterations. This observation is consistent with the monotonic acceptance rule, but it is not a claim of global optimality.

Increasing the total number of ORIS units from $N = 36$ to 100 improves the plotted sum rate by providing more reflected-link choices. Increasing the LED count also improves spatial diversity and the available optical-power budget.

To further address hardware realism, Table 5 reports lightweight numerical stress tests around the nominal setting $\rho = 0.95$, $\psi_c = 60°$, and $\sigma_\theta = 10°$ at 35 dB. The results are normalized by the nominal weighted sum rate. Lower reflection efficiency and narrower FoV reduce the absolute gain, as expected, while the optimized ORIS-assisted scheme remains above the no-ORIS baseline trend in Fig. 5(b). Increasing the

TABLE 5. Sensitivity of normalized weighted sum rate to practical parameters at 35 dB. The nominal setting $(\rho, \psi_c, \sigma_\theta) = (0.95, 60°, 10°)$ is normalized to 100%.

Stress factor	Low setting	Nominal	High setting
Reflection coefficient ρ	89.4% (0.75)	100.0% (0.95)	–
Receiver FoV ψ_c	90.1% (45°)	100.0% (60°)	102.3% (75°)
Orientation std. σ_θ	101.6% (5°)	100.0% (10°)	95.1% (15°)

orientation standard deviation from $10°$ to $15°$ causes a visible but moderate degradation, indicating that the statistical-CSI design remains useful beyond the nominal sitting-user regime.

5.2. Comparison with Baseline Benchmarks

The single-user experiment in Section 2.4 uses the Shannon expression only as a motivation plot. The multi-user evaluation uses the statistical IM/DD surrogate $\bar{R}_j = (B/2)\log_2(1 + e\widehat{\mathrm{SINR}}_j/(2\pi))$. Each LED shares the optical budget $P_{\max}^{\mathrm{opt}}$ among at most $N_{\max}$ users, and the N total ORIS units satisfy C8 and C9.

Three baselines are considered. PAO allocates optical power in proportion to $\hat{h}_{i,j,j}$, associates users by LoS gain, and applies local ORIS swaps. TDMA serves users in equal orthogonal slots while retaining ORIS optimization. No-ORIS sets $H_{i,n,j}^{\mathrm{ORIS}} = 0$ and optimizes only **P** and **F**.

Figure 5(b) compares the results. At 35 dB, the plotted aggregate rates are about 125 Mbps for the proposed method, 110 Mbps for PAO, and 80 Mbps for TDMA. TDMA is lower in this test because equal orthogonal slots do not exploit power-domain multiplexing.

The plotted gap grows with SNR over the tested range, indicating that joint NOMA and ORIS updates manage interference more effectively than the tested heuristics in these simulations.

At 40 dB, the No-ORIS curve is near 90 Mbps and shows saturation. The comparison indicates that reflected paths can mitigate orientation-related LoS attenuation in the tested geometry.

6. CONCLUSIONS

This paper has investigated statistical-CSI-based resource allocation for ORIS-assisted multi-cell NOMA-VLC networks under random user orientations. The joint optical-power, user-association, and ORIS-activation problem was formulated as a mixed-integer non-convex program and addressed via a BCD framework combining fractional programming, successive convex approximation, and semidefinite relaxation.

The simulations show higher statistical-CSI surrogate rates than the tested orthogonal and heuristic baselines. Future work will consider lower-complexity ORIS control, dynamic mobility, non-stationary orientation models, and learning-based updates.

ACKNOWLEDGEMENT

This work was supported by the Beijing Information Science and Technology University (BISTU) Research Fund Program for Young Scholars under Grant BISTU22QN010.

REFERENCES

[1] Yoshida, K., C. Chen, H. Haas, G. A. Turnbull, and I. D. W. Samuel, "RGB-single-chip OLEDs for high-speed visible-light communication by wavelength-division multiplexing," *Advanced Science*, Vol. 11, No. 47, 2404576, Dec. 2024.

[2] Komine, T. and M. Nakagawa, "Fundamental analysis for visible-light communication system using LED lights," *IEEE Transactions on Consumer Electronics*, Vol. 50, No. 1, 100–107, Feb. 2004.

[3] Wu, X., M. D. Soltani, L. Zhou, M. Safari, and H. Haas, "Hybrid LiFi and WiFi networks: A survey," *IEEE Communications Surveys & Tutorials*, Vol. 23, No. 2, 1398–1420, 2021.

[4] Khan, W. U., E. Lagunas, A. Mahmood, Z. Ali, M. Asif, S. Chatzinotas, and B. Ottersten, "Integration of NOMA with reflecting intelligent surfaces: A multi-cell optimization with SIC decoding errors," *IEEE Transactions on Green Communications and Networking*, Vol. 7, No. 3, 1554–1565, Sep. 2023.

[5] Liu, Z., F. Yang, S. Sun, J. Song, and Z. Han, "NOMA-based multi-cell VLC systems with optical intelligent reflecting surface: Resource allocation for energy efficiency maximization," *IEEE Journal on Selected Areas in Communications*, Vol. 43, No. 5, 1691–1705, May 2025.

[6] Fang, W., W. Chen, Q. Wu, K. Wang, S. Zhang, Q. Liu, and J. Li, "Reconfigurable intelligent surface assisted free space optical information and power transfer," *IEEE Internet of Things Journal*, Vol. 11, No. 18, 30 260–30 277, Sep. 2024.

[7] Xie, X., F. Fang, and Z. Ding, "Joint optimization of beamforming, phase-shifting and power allocation in a multi-cluster IRS-NOMA network," *IEEE Transactions on Vehicular Technology*, Vol. 70, No. 8, 7705–7717, Aug. 2021.

[8] Xie, Z., W. Yi, X. Wu, Y. Liu, and A. Nallanathan, "STAR-RIS aided NOMA in multicell networks: A general analytical framework with gamma distributed channel modeling," *IEEE Transactions on Communications*, Vol. 70, No. 8, 5629–5644, Aug. 2022.

[9] Soltani, M. D., A. A. Purwita, Z. Zeng, H. Haas, and M. Safari, "Modeling the random orientation of mobile devices: Measurement, analysis and LiFi use case," *IEEE Transactions on Communications*, Vol. 67, No. 3, 2157–2172, Mar. 2019.

[10] Arfaoui, M. A., M. D. Soltani, I. Tavakkolnia, A. Ghrayeb, C. M. Assi, M. Safari, and H. Haas, "Measurements-based channel models for indoor LiFi systems," *IEEE Transactions on Wireless Communications*, Vol. 20, No. 2, 827–842, Feb. 2021.

[11] Cai, W., R. Liu, M. Li, Y. Liu, Q. Wu, and Q. Liu, "IRS-assisted multicell multiband systems: Practical reflection model and joint beamforming design," *IEEE Transactions on Communications*, Vol. 70, No. 6, 3897–3911, Jun. 2022.

[12] Qian, L., F. Wu, D. Wang, N. Huang, and Z. Xu, "Optical RIS-aided covert visible light communications," *IEEE Transactions on Vehicular Technology*, Vol. 74, No. 7, 11 518–11 523, 2025.

[13] Mushfique, S. I., A. Alsharoa, and M. Yuksel, "Optimization of SINR and illumination uniformity in multi-LED multi-datastream VLC networks," *IEEE Transactions on Cognitive Communications and Networking*, Vol. 6, No. 3, 1108–1121, Sep. 2020.

[14] Shen, K. and W. Yu, "Fractional programming for communication systems — Part I: Power control and beamforming," *IEEE Transactions on Signal Processing*, Vol. 66, No. 10, 2616–2630, May 2018.

[15] Shen, K. and W. Yu, "Fractional programming for communication systems — Part II: Uplink scheduling via matching," *IEEE Transactions on Signal Processing*, Vol. 66, No. 10, 2631–2644, May 2018.

[16] Yang, Y., Y. Yang, M. Chen, C. Feng, H. Xia, S. Cui, and H. V. Poor, "Joint LED selection and precoding optimization for multiple-user multiple-cell VLC systems," *IEEE Internet of Things Journal*, Vol. 9, No. 8, 6003–6017, Apr. 2022.

[17] Mmbaga, P. F., J. Thompson, and H. Haas, "Performance analysis of indoor diffuse VLC MIMO channels using angular diversity detectors," *Journal of Lightwave Technology*, Vol. 34, No. 4, 1254–1266, Feb. 2016.

[18] Singh, A., H. B. Salameh, M. Ayyash, and H. Elgala, "Performance analysis of OIRS-aided indoor VLC systems under dynamic human blockages and random UE orientation," *IEEE Internet of Things Journal*, Vol. 11, No. 20, 33 110–33 119, Oct. 2024.

[19] Abdelhady, A. M., A. K. S. Salem, O. Amin, B. Shihada, and M.-S. Alouini, "Visible light communications via intelligent reflecting surfaces: Metasurfaces vs mirror arrays," *IEEE Open Journal of the Communications Society*, Vol. 2, 1–20, 2020.